

The response of Saturn's dawn field-aligned currents to magnetospheric and ring current conditions during Cassini's proximal orbits: Evidence for a Region 2 response at Saturn

G. J. Hunt^{*1}, G. Provan², T. J. Bradley², S. W. H. Cowley², M. K. Dougherty¹, E. Roussos³

¹ Blackett Laboratory, Imperial College London, London, SW7 2BW, UK

² Department of Physics and Astronomy, University of Leicester, Leicester, LE1 7RH, UK.

³ Max Planck Institute for Solar System Research, Göttingen, Germany

Three key points –

- 1) We combine datasets for Saturn's northern auroral field-aligned currents, magnetospheric compression state and total ring current.
- 2) For compression events the downward current sheet at dawn increases in strength with the total ring current and higher energy protons.
- 3) We conclude that there is an enhanced dawn downward current (~ 0.5 MA/rad), which is akin to a Region 2 current system at Earth.

Draft A: Submitted to *JGR* on 6th August 2021

Draft B: Submitted to *JGR* on 27th March 2022

*Corresponding author (gregjhunt1@gmail.com)

Abstract

Cassini's 2017 proximal orbits provided the opportunity to examine the auroral field-aligned currents in the northern hemisphere dawn sector in relation to wider magnetospheric conditions. We combine three recent studies to examine the response of the dawn region auroral field-aligned currents and the azimuthal ring currents to compressions and expansions of the Saturnian magnetosphere. For compressions of Saturn's magnetosphere resulting in tail reconnection, the currents within the downward current sheet, located equatorward of the main auroral oval, increases in strength with increasing total ring current and location of the peak downwards current moves inwards towards Saturn. While the inverse relation occurs during intervals of quiet or expanded magnetospheric conditions. During compression events there is an increase in the energetic particle intensities, in particular in the protons (35-506 keV), within the downward current region. This current system is akin to an Earth-like 'region 2' field aligned current within Saturn's magnetosphere, with tail reconnection occurring when the magnetosphere is compressed resulting in a partial nightside ring current closed by a downward current near to dawn. Within the upward current sheet, mapping to Saturn's main auroral oval, both non-rotating subcorotating current and the rotating Planetary Period Oscillations (PPOs) currents flow. The upward current is strongly modulated by the PPOs but also increases in strength, with enhanced high-energy protons, during intervals of magnetospheric compressions and tail reconnection. We conclude that the enhanced plasma injected into the midnight-dawn sector during tail reconnection events results in an enhanced subcorotation current system.

1. Introduction

Field-aligned currents are fundamental in transferring momentum within a planetary magnetosphere by coupling the planet's ionosphere to its magnetosphere. For Saturn's magnetosphere these current systems have been extensively studied through Cassini magnetometer data (Bradley et al., 2018; Bunce et al., 2008; Cowley et al., 2008; Dougherty et al., 2004; Hunt et al., 2014, 2015, 2016, 2018, 2020; Southwood & Kivelson, 2007; Talboys et al., 2009a; Talboys et al., 2009b; Talboys et al., 2011). Observations indicate that two principal large-scale field-aligned current systems are present. The first will be referred to as the non-PPO current system throughout this paper. This current system is axi-symmetric and is associated with the velocity shear of magnetospheric plasma close to the open-closed field line boundary. Previous studies have suggested that this non-PPO current system typically comprises of four distinct current sheets (Hunt et al., 2014, Hunt et al., 2018). Moving equatorwards from the pole, we first observe a distributed downward field-aligned current of ~ 1.1 MA per radian of azimuth flowing over the polar cap, indicative of significant plasma sub-corotation. Equatorwards of this, at $\sim 17^\circ$ - 19° ionospheric colatitude, we next observe the main auroral upward current carrying ~ 2.3 MA rad^{-1} that maps to the outer hot plasma region in Saturn's magnetosphere, colocated with Saturn's UV auroral oval. Equatorwards of this main upward current region, we observe two subsidiary downward-and-then-upward current sheets of ~ 0.5 MA rad^{-1} . To date there is no clear signature in the equatorial plasma angular velocity profiles to explain these two secondary subsidiary current sheets.

The existence of the second large-scale current system, the PPO field-aligned currents, was first alluded to by observations from Pioneer-11, Voyager-1 and Voyager-2, showing that despite the near-perfect axisymmetry of Saturn's internal planetary magnetic field (e.g., Dougherty et al., 2018), oscillations near the planetary rotation period are ubiquitous throughout Saturn's magnetosphere (e.g. Carbary & Mitchell, 2013). Cassini observations of modulations in the powerful Saturn kilometric radiation (SKR) emissions have shown that there are in fact two such planetary period oscillation (PPO) systems present, one related to each polar hemisphere, that rotate about the planetary axis with slightly different periods (Kurth et al., 2008; Gurnett et al., 2009a, 2009b). The two PPO oscillations are associated with two large-scale current systems, one rotating at the period of the Northern PPO oscillation and the other at the period of the Southern PPO oscillation (Hunt et al., 2018, 2018). The PPO current systems have a $m=1$ axial symmetry with rotating

65 sheets of upward and downward current on either side of the polar region (separated by 180° of PPO phase).
 66 The two PPO up-and-down current sheets flow at ionospheric colatitude of $\sim 17.5^\circ$ - 20° , overlapping the
 67 main upward and subsidiary downward current system and carry comparable upward and downward currents
 68 peaking at $\sim 1.7 \text{ MA rad}^{-1}$. This result in both the overall total current, and the current layer colatitude, being
 69 modulated at the PPO periods.

70 The proximal orbits of the Cassini mission's Grand Finale in 2017 provided the opportunity to examine the
 71 auroral field-aligned currents in the dawn sector, 06-08h local time (LT), of Saturn's magnetosphere. The
 72 initial observations were reported by Hunt et al. (2020), such that we only provide a brief summary here. To
 73 begin with they identified the main field-aligned current sheets in the auroral region, namely the main
 74 upward current associated with the aurora and a downward current equatorward of this. On a statistical level
 75 Hunt et al. (2020) separated the non-PPO and PPO field-aligned current systems. By comparing the proximal
 76 orbits with the F-ring orbits it was shown that there was an enhanced non-PPO upward current within the
 77 dawn sector (proximal orbits) compared with the noon sector (F-ring orbits). They proposed that the
 78 increased dawn upward current could be related to increased plasma flows in the outer magnetospheric dawn
 79 sector.

80 The magnetospheric and heliospheric conditions during Cassini's Grand Finale were determined by Bradley
 81 et al., (2020). To infer heliospheric conditions they combined modeled solar wind data propagated from 1AU
 82 to Saturn (Tao et al. 2005; Zieger & Hansen 2008) with Cassini energetic particle measurements which
 83 detect the fluxes of solar energetic particles and galactic cosmic ray that penetrate into Saturn's
 84 magnetosphere (Roussos, Jackman, et al., 2018 and Roussos, Krupp et al. 2018). In addition, they used in-
 85 situ and remote observations of Saturn's auroral regions to identify the response to solar wind compressions
 86 of Saturn's magnetosphere. For the list of compression events over the Grand Finale see Tables 1 and 2 of
 87 Bradley et al., (2020). They showed clear responses to solar wind compression events, with compression
 88 and deflection of the magnetic field and particle injections. When the PPO systems were in anti-phase during
 89 solar wind compressions they also reported a larger response within the SKR emissions. Bradley et al. (2020)
 90 explain how such anti-phase PPO conditions resulted in a thin plasma/current sheet making the conditions
 91 for reconnection in the tail more favorable.

Recently, Provan et al., (2021) also performed fits to magnetic field observations of the nightside ring current during the proximal orbits to determine its properties. The fits were applied to ~ 1 day of data either side of periapsis with the central ~ 8 hr interval excluded. The crossing of the northern auroral field-aligned currents occurred ~ 1.5 -2 hours before periapsis, placing them just between the fitting intervals used by Provan et al., (2021), thus making their ring current parameters approximately concurrent with the field-aligned current observations from Hunt et al. (2020). Provan et al., (2021) found that the ring current was driven by both external and internal factors, namely solar wind compressions and the PPOs. They found that during solar wind compressions of the magnetosphere combined with when the beat phase of the two PPO systems was approximately 180° e.g., the systems were in anti-phase, the nightside ring current strengthen and thickened. This suggests a significant partial ring current formed on the nightside in response to the injected hot plasma from tail reconnection. They proposed that this partial ring current could partly close via field-aligned currents into the ionosphere.

In Figure 1 we illustrate the current systems as described above, namely the non-PPO current system, PPO current system, and the proposed partial ring current. To begin Figure 1a shows the ionospheric projection of the system as viewed from the north. Moving equatorward from the pole the light blue circle represent the distributed downward subcorotation current and the pink circle at slightly larger co-latitudes represents the upward directed subcorotation currents forming the main auroral oval. The green circled crosses and dots represent the northern PPO-related field-aligned currents with the circled crosses indicated current flowing into the ionosphere (downward) and the circled dots show current flowing out of the ionosphere (upward). The key northern PPO phase meridians are shown by the values around the edge. These are defined by $\Psi_N(\varphi, t) = \Phi_N(t) - \varphi$, where Φ_N is the global PPO phase which give the angle from noon of the principal meridian of the northern system, $\Psi_N = 0^\circ$, where the near-equatorial quasi-uniform PPO perturbation field points radially outward from the planet. The local phases at the observation points are then obtained by subtracting the azimuth of the observation point φ similarly measured from noon positive towards dusk. To make an analogy in order to explain the global and local phases more clearly, the global phases are akin to Universal Time on Earth, while the local phases are the akin to a longitude system with $\Psi_{N,S} = 0^\circ$ serving the same function as the Greenwich Meridian. The global phases $\Phi_{N,S}(t)$ have been determined over the proximal orbits by Provan et al. (2018). For the northern PPO current system, the main

currents flow into the ionosphere (downward) at $\Psi_N = 270^\circ$ and out of the ionosphere (upward) at $\Psi_N = 90^\circ$.

Figure 1b and 1c show the current systems as viewed in the 90° - 270° Ψ_N meridian, such that $\Psi_N = 0^\circ$ is into the page and it is in the direction of noon. The color scheme is the same as Figure 1a. The grey ring illustrates Saturn's magnetospheric ring current with the total current being, I_T , flowing from dusk to dawn. Figure 1b is the configuration for normal magnetospheric conditions, while Figure 1c illustrates the proposal partial ring current and associated closure currents as proposed by Provan et al. (2021) as shown by the red arrows. Given Saturn's magnetic field and rotation of plasma this partial current system, would be closed via field-aligned currents that are upward from the ionosphere in the dusk sector and downward currents in the dawn sector, as shown in Figure 1c. This response would be akin to Earth's region 2 field-aligned current system, albeit oppositely directed, due to the oppositely directed planetary magnetic field. At Earth this region 2 current system increases in response to geomagnetic activity where a partial nightside ring current forms, and is closed via upward field-aligned current at dawn and downward current in the dusk sector (e.g. Cowley 2000, Coxon et al., 2015).

A possible region 2 current has been inferred from the divergence of the current densities in the equatorial regions of both Jupiter and Saturn's magnetosphere (Khurana 2001; Lorch et al., 2019; Martin & Arridge, 2019). These studies have all shown enhanced currents flowing out of the post-midnight/dawn equatorial region which would therefore be downward into each hemisphere's ionosphere. The proximal orbits of Cassini allow us to determine if a Region 2 current forms in Saturn's dawn auroral region in response to magnetospheric conditions.

In this paper we combine the results from the three studies outlined above (Hunt et al., 2020; Bradley et al., 2020; Provan et al., 2021) and in-situ plasma measurements from Cassini's Low Energy Magnetospheric Measurements System (LEMMS) of the Magnetospheric Imaging Instrument (MIMI) to investigate the response of the northern hemisphere dawn auroral field-aligned currents to magnetospheric conditions, specifically solar wind compressions and the resultant intensifications of the nightside ring current.

2. Data Overview

In this section we will discuss the data employed within this study. Figure 2 shows an example of the orbit geometry during the proximal orbits of the Cassini spacecraft. Figure 2a shows the spacecraft trajectory of

Cassini Revolution (Rev) 273 in cylindrical coordinates (ρ, z) , where z is aligned with the spin/magnetic axis of the planet and ρ is the perpendicular distance from it. The magnetic field lines are determined from the first 3 terms of the Dougherty et al., (2018) internal field model combined with the Bunce et al., (2007, 2008) ring current model with the subsolar magnetopause standoff distance set to $22 R_S$. The grey shaded region highlights the field region that carries the main auroral region field-aligned currents. Cassini quickly passed through the auroral field lines in a north to south direction on the inbound pass. Figure 2b shows the ionospheric footprint of Cassini determined from the same magnetic field model as shown in Figure 2a. We show two trajectories, Revs 273 and 289, which occurred towards the beginning and end of the proximal orbits, respectively. Over the course of the proximal orbits Cassini traversed the field lines which map to the northern main auroral region between $\sim 06\text{-}08$ h LT.

In this study we will employ three datasets from Hunt et al., (2020), Bradley et al., (2020), and Provan et al., (2021), these data are provided in Table 1. In addition, we use in-situ plasma measurements from Cassini MIMI/LEMMS within the field-aligned current region. For full details of the Cassini MIMI/LEMMS instrument see Krimigis et al. (2004) and Armstrong et al. (2009).

To begin our discussion, we will compare two passes through the northern auroral region and will use these examples to familiarize ourselves with the data for later analysis. We have chosen Revs 273 and 289, identified by Bradley et al., (2020) and Provan et al., (2021) as normal and compressed magnetosphere conditions, respectively. Figures 3a-3d shows the Cassini in situ data from the northern hemisphere dawn sector auroral region for Rev 273, while Figures 3e-3h show in-situ data for Rev 289. In Figure 3a we show the horizontal ionospheric meridional current, I_m , per radian of azimuth (MA/rad) flowing at the feet of the spacecraft field lines. This is calculated from Cassini observations of the azimuthal magnetic field, B_ϕ , and by employing Ampère's law to a circular path about the planetary spin/magnetic axis through the observation point at radius ρ , giving

$$I_m = -\frac{\rho B_\phi}{\mu_0}, \quad (1)$$

where μ_0 is the permeability of free space. This is defined such that a positive I_m is directed from the northern pole towards the equator. This method of calculating I_m is well established, for full details see Hunt et al., (2014, 2015). As Cassini moved equatorward to larger colatitudes (see Figure 3d) the positive I_m is

resultant from a negative azimuthal field structure, indicative of a swept-back (lagging) field in the northern hemisphere associated with the polar distributed downward current (Hunt et al., 2014, 2015, 2020). The first significant negative gradient indicates the main upward auroral current. These first two vertical dashed lines mark the boundaries of the upward auroral current which was determined by Hunt et al., (2020), where the direction of the field-aligned current is given by the red arrow. Current continuity then requires that the total field-aligned current per radian of azimuth flowing between two colatitude points, θ_{iN1} and θ_{iN2} , where $\theta_{iN2} > \theta_{iN1}$, is given by

$$I_{\parallel} = -(I_m(\theta_{iN2}) - I_m(\theta_{iN1})). \quad (2)$$

This is defined such that a positive I_{\parallel} indicates an upward field-aligned current direction parallel to the background magnetic field in the northern hemisphere. Below we will examine how this current system is a combination of the PPO and the non-PPO field-aligned currents, as described above. In Figure 3a the following positive I_m gradient equatorward of the auroral upward current is the downward current sheet. The current sheet is marked by the second and third vertically dashed lines, with the direction of the field-aligned current shown by the red arrow. In section 3 we will compare the I_{\parallel} current flowing within these sheets with the total ring current from the fits performed by Provan et al. (2021).

Figures 3b and 3c show the intensities of the electron and proton channels from LEMMS, respectively. Specifically, we show electron channels E0 – E2 (110 – 1350 keV) and proton channels A1 – A4 (35 – 506 keV), these are the same channels as used by Bradley et al., (2020) and Provan et al., (2021). Each channel is color-coded as shown in the figure. Figure 3e-3h are in the same format and display the data from Rev 289 identified by Bradley et al. (2020) as a compressed magnetosphere and auroral storm event. Given the high latitude nature of the observations LEMMS can monitor the charged particles with high field-aligned velocity component given that particles without this would not have reached the high latitude regions. We also note that these protons channels can also detect heavier ions as shown by Armstrong et al., (2009), however, above 100 keV the channels are typically dominated by protons. Furthermore, as the LEMMS measurements used within this study are from the high latitude magnetosphere therefore we expect less heavier ions present as they tend to be confined to the equatorial magnetosphere (Sittler et al. 2008). To note, we suspect that the spikes within the proton intensities at ~04:45 (Figure 3c) and ~13:55 (Figure 3g) are due

to magnetospheric dynamics within or close to the OCB and the associated downward current within this region, however, further investigation is outside the scope of this paper.

By comparing Revs 273 and 289 we can start to explore the differences within the auroral region between the normal and compressed magnetospheric response. Firstly, the I_m profile shows for the compressed event (Rev 289) there is a larger total current within both the upward and downward current sheets. Secondly, there is a noticeable increase in the colatitude width of the downward current for the compression case, as indicated by the colatitude range between the second and third current sheet boundaries in Figure 3h compared to Figure 3d. Finally, in the energetic particle measurements, the electron intensities are broadly similar in the auroral region albeit with larger intensities at lower latitude in Figure 3f compared to Figure 3b. There is an order of magnitude increase in the proton intensities for the compressed case therefore showing a clear response within the downward current sheet during the compression case on Rev 289. This suggests there is a response in the auroral region, in particular in the strength of the currents and proton intensities to a compression of the magnetosphere.

To explore this further we combine all the field-aligned current observations ($I_{||}$) from Hunt et al., (2020) with the magnetospheric state determined by Bradley et al., (2020), and the total ring current values (I_T) from Provan et al. (2021), see Table 1 for the values. As described in detail by Provan et al. (2021), these authors examined Cassini's passage through Saturn's ring current during Cassini's proximal orbits. Utilizing the Connerney et al. (1981, 1983) ring current model, they calculated the best-fit ring current's thickness, radial extent and the current density parameter on a rev-by-rev basis, assuming that the ring current comprises of four current discs, $n=1$ to 4. The inner and outer cylindrical radii of each of the four discs is denoted by $R_{1,n}$ and $R_{2,n}$ and its half thickness by D_n . The total current of the ring current, I_T , is then calculated for each rev using

$$I_T = 2I_0 \sum_{n=1}^{n=4} D_n \ln \left(\frac{R_{2,n}}{R_{1,n}} \right) \quad (3)$$

where $\mu_0 I_0$ is the best-fit current density parameter of the ring current.

Furthermore, we employ the field-aligned current boundaries to determine the average energetic particle intensities in that field region. We include all Revs possible from Rev 271-292, however, noting that Revs

272, 277, 280 are not included either due to data gaps (Rev 277) or clear field-aligned current sheets not being identified (Revs 272, 280).

3. Comparison between the Field-Aligned Currents and Total Ring Current with Magnetospheric Compression State

To begin, in Figure 4a, we reproduce a plot from Provan et al. (2021), their Figure 14a, showing the total ring current current I_T , determined on a rev-by-rev basis, and plotted versus magnetospheric standoff distance, R_M . The magnetopause stand-off distance is estimated using the solar wind dynamic pressure propagated to Saturn using an MHD code initialized OMNI (Operating Missions as a Node on the Internet) data obtained near ~ 1 AU (Tao et al., 2005, also discussed in Bradley et al., 2020) inputted into the model of Kanani et al. (2010). The points are color-coded by magnetospheric state from Bradley et al. (2020) and Provan et al., (2021), with green indicating normal magnetospheric conditions, orange a partially-compressed magnetosphere, red a compressed magnetosphere and blue an expanded magnetosphere. The mean value of the total current is overplotted as a dashed line. Provan et al. (2021) stated that the total current carried by the nightside ring current is similar all times, except during the red compressed magnetosphere intervals. Apart from these times, the mean total current $I_T = 16.3 \pm 1.0$ MA. During major magnetospheric compression events, an increase in the thickness of the ring current results in an increase in the total ring current by $\sim 20\%$ to $I_T = 20.0 \pm 1.4$ MA.

Figure 4b presents the total current within the downward current sheet per radian of azimuth, $I_{||}$, determined on a rev-by-rev basis by Hunt et al., (2020), plotted in the same format as Figure 4a. The mean value of $I_{||}$ for the entire dataset is shown as a horizontal dashed line, equal to 0.93 ± 0.37 MA rad^{-1} . It is clear that the current in the downward current sheet when the magnetosphere is compressed or partially compressed is close-to or above the mean value. The average value of $I_{||}$ in the downward current sheet for a compressed magnetosphere (red values) is 1.17 ± 0.32 MA rad^{-1} , while the mean $I_{||}$ for the expanded magnetosphere (blue values) is 0.66 ± 0.12 MA rad^{-1} . When the magnetosphere is compressed or partially compressed (red and orange circles), $I_{||} = 1.20 \pm 0.42$ MA rad^{-1} , whilst when the magnetosphere is in an expanded or normal state (green and blue), $I_{||} = 0.80 \pm 0.28$ MA rad^{-1} .

Figure 4c presents θ_{IN} , the ionospheric co-latitude of the center of the downward current region mapped to the Northern hemisphere ionosphere. The mean value $\bar{\theta}_{IN}=18.08\pm1.17^\circ$ is shown as a horizontal dashed line. From a visual inspection of the plot it seems clear that, in general, the red and orange circles are close-to or above this mean value. When the magnetosphere is compressed or partially-compressed $\bar{\theta}_{IN}=18.49\pm1.51^\circ$, mapping to $8.2 R_s$ in the equatorial plane, while when the magnetosphere is in a normal or expanded state is $\bar{\theta}_{IN}=17.84\pm0.97^\circ$, mapping to $9.2 R_s$ in the equatorial plane. Thus, the downward current region moves inwards towards Saturn by approximately $1 R_s$ when the magnetosphere is compressed or partially compressed compared to when the magnetosphere is in a normal or expanded state.

Figure 4d shows the total current within the upward current sheet per radian of azimuth, $I_{||}$. The horizontal dashed line shows the mean value of $2.01 \pm 0.62 \text{ MA rad}^{-1}$. There is a fair amount of variability of the upward current however the average value of $I_{||}$ when the magnetosphere is compressed (red values) is $2.32\pm0.58 \text{ MA rad}^{-1}$, which is significantly larger than the mean upward $I_{||}$ observed during an expanded magnetosphere (blue) of $1.56\pm 0.46 \text{ MA rad}^{-1}$. We note that typically the upward current sheet maps to the outer edge of the ring current and close to the OCB (Hunt et al., 2014, 2015, 2020), thus we may not necessarily expect a strong relationship between the two currents.

Finally, Figure 4e presents θ_{IN} , the ionospheric co-latitude of the center of the upward current region mapped to the Northern hemisphere ionosphere. The mean value $\bar{\theta}_{IN}=16.20\pm0.48^\circ$, which maps to $13.2 R_s$ in the equatorial planet. When the magnetosphere is expanded (red values) $\bar{\theta}_{IN}=16.34\pm0.54^\circ$, whilst when the magnetosphere is compressed (blue values), $\bar{\theta}_{IN}=16.07\pm0.48^\circ$. Thus, the radial position of the upward current region is not significantly altered by compressions or expansions of Saturn's magnetosphere.

In Figure 5 we further examine the relationship between the total ring current current, I_T , and the field-aligned currents in the upward and downward current sheet current by plotting I_T versus downward $I_{||}$ (Figure 5a) and upward $I_{||}$ (Figure 5b). The figures are color coded by magnetospheric conditions as before. In both figures we also present the mean value for the compressed magnetosphere (large red circle), compressed and partially-compressed magnetosphere (large red circle with an orange center), expanded magnetosphere (large blue circle) and normal or expanded magnetosphere (large blue circle with a green center). As stated above there is a clear relationship between compressed and partially compressed magnetospheric conditions, and

enhanced currents flowing in both the upward and downward current sheets. This dependence is particularly clear between the total ring current, and the downward current demonstrated by the cluster of compressed (red) points at high I_T and $I_{||}$ values compared normal and expanded conditions (green and blue). Indeed, the mean total current in the downward current sheet is approximately doubled when the magnetosphere is compressed compared to when it is expanded. The one compressed event which does not agree here is Rev 276. Provan et al., (2021) indicated that the compression during this Rev occurred during the fitting interval for the ring current and therefore was excluded from further analysis. We have included it here as the $I_{||}$ value is comparable to other compression events, implying that the field-aligned currents are reacting to the compression event.

Provan et al. (2021) found that the total current within the ring current is enhanced when the magnetosphere is compressed and tail reconnection occurs, consistent with the formation of a partial ring current populated by hot plasma. Here we find a related increase in the $I_{||}$ flowing in the downward current sheet. This indicates that the partial ring current closes via the downward current sheet in the dawn sector, with this current sheet mapping equatorward of the main auroral oval. If we suppose that this downward current occupies ~ 2 rad in azimuth within the dawn magnetosphere. It then follows for low I_T (less than ~ 16 MA) values, the closure current would come to ~ 1.6 MA, which is $\sim 10\%$ of the ring current. For values of higher I_T (greater than ~ 18 MA) values the closure current may go up to ~ 3 MA, which is $\sim 15\text{-}20\%$ of the ring current and therefore removing a significant fraction of the additional current during compression events (Revs 274, 276, 288, and 289). We also find an increase in $I_{||}$ in the upward current sheet of the main auroral oval when tail reconnection occurs.

4. LEMMS Observations and Discussion

As seen in the comparison between a normal and compressed magnetosphere in section 2 (Figure 3) we observe a clear difference in the plasma populations, in particular for the high energy proton channels. To explore this further we calculate the mean of the LEMMS proton (A1-A4) and electron (E0-E2) intensities within the downward and upward current sheet for each of the 19 orbits included in this study. Examples of these downward and upward current sheet for Rev 273 and 289 are shown in Figure 3a-d and in Figure 3e-h, respectively. The upward current region is bounded by the first and second vertical dashed lines and marked by an upward red arrow, and the downward current region by the second and third vertical dashed line and

marked by a downward red arrow in each figure. The results of this averaging are shown in Figure 6a (downward electrons), 6b (downward protons), 6e (upward electrons) and 6f (upward protons). The vertical lines mark compressed (red) and part compressed (orange) magnetospheric conditions. In Figure 6a, showing the average electron fluxes in the downward current sheet, we observe some orbit-to-orbit variability with a possible response to the ongoing compression events resulting in enhanced electron intensity. The proton average intensities in the downward current sheet as presented in Figure 6b show a clearer response to the compressions events as indicated by the vertical dashed lines. During each compression interval there are elevated average intensities across the A1-A4 channels. In particular, there are significant increases (\sim an order of magnitude) in the protons channels. Figure 6e (6f) present the electron (proton) intensity in the upward current region. It is clear that the electron intensity in the upward current sheet is lower than in the downward current sheet. There is some evidence of an increase in the proton intensity in the upward current sheet during the red and orange revs, but a similar effect is not observed for the electrons. Figure 6c (6g) presents the ionospheric co-latitude of the central downward (upward) current region as a black line, and the corresponding equatorial radial distance in the magnetosphere (red line). Typically, for larger radial distances, the electron intensities decrease, this is board agreement of the electron populations as determined by Schippers et al., (2008) who noted a boundary at ~ 9 RS which is close to region the downward field-aligned current maps to. In addition, this region is close to the plasmopause, the boundary between cooler and hotter plasma in Saturn equatorial magnetosphere, as identified by Thomsen and Coates (2019). One Rev to note is Rev 283, within the downward current sheet there are high proton intensities whilst not being related to a compression event. This particular Rev was also noted by Bradley et al., (2020) for this (see their S1 supporting information). They observed that during Rev 283 [there were intense PPO-modulated short-lived bursts of SKR. This combined with the enhanced energetic particle fluxes is indicative of strong PPO-modulated Vasyliunas cycle activity occurring, under approximately quadrature PPO beat phase conditions. This process enhances the hot plasma and energetic particle content of the closed magnetosphere field \(e.g. Cowley et al., 2004, 2005; Thomsen & Coates, 2019\), thus explaining the high intensity observed here for Rev 283 within the downward current which maps to this region.](#)

Figure 6d (6h) shows the local PPO phases for both the northern and southern systems, $\Psi_{N,S}$, determined at the center of the downward (upward) current sheet. These are defined as described in Section 1. The PPO

beat phase ($\Phi_B = \Psi_N - \Psi_S$) are denoted by the black crosses. As discussed by Bradley et al., (2020) and Provan et al., (2021), the largest responses to magnetospheric compression events occur when the two PPO systems are in antiphase, where the term antiphase is used when the two PPO systems are rotating within $\pm 90^\circ$ of antiphase i.e. $\Phi_B = 180 \pm 90^\circ$, such conditions are Figures 6d and 6h as shaded orange horizontal bars. As Provan et al. (2021) reported, the four red revs (highlighted by solid red lines) all occur during PPO antiphase conditions when magnetospheric reconnection is preferred to occur.

In Figure 7 we further examine the relationship between electron and proton intensity in the upward and downward current sheets, and the total ring current current. Figure 7a (7b) presents the proton (electron) intensity plotted with respect to the total ring current current in the downward current sheet, and Figures 7c (7d) in the upward current sheet. The outer edge of the circle is color coded by energy channels, while the center of the circle is color coded by magnetospheric state. We can see that the protons in the upward and downward current sheet are enhanced during the red revs when Saturn's magnetosphere is compressed, tail reconnection occurs, and a partial ring current is formed consistent with injected hot protons. We also observe enhanced electron intensity in the upward current sheet but decreased electron intensity in the downward current sheet as the total ring current increases.

The enhanced intensity of energetic protons within the downward current carrying region is in good agreement with energetic plasma injected into the ring current following magnetotail reconnection. This forms a partial ring current and increases I_T as observed by Provan et al. (2021). The injected plasma then rotates into the dawn sector, as shown by previous studies of injection events (e.g, Mitchell et al., 2009; Thomsen and Coates 2019; Kinrade et al., 2020; and Bradley et al., 2020). We observe that on the field lines mapping to the ring current region ($\sim 7-12 R_s$) in the equatorial magnetosphere an enhanced downward current is present during the compression events. Sergis et al., (2017) showed that within the dawn sector the ring current is strongly pressure gradient driven, which is consistent with the flow of hot magnetospheric plasma following reconnection down tail. We further observe that when the magnetosphere is compressed, and the partial ring current is formed the downward current region is displaced inwards. A similar result was observed within the orbit of Enceladus by Kellett et al. (2011), who compared the ring current during an interval of solar wind compression with an interval when the magnetosphere was less compressed (their Figure 11). They stated that in the outer region (beyond $8-9 R_s$) the currents were weaker by a factor up to

~2 when the magnetosphere was compressed. However, similarly to the observations presented here, inside ~10 R_s the peak in current density moves inwards from 9 R_s to 7 R_s when the magnetosphere was compressed. We conclude that the partial ring current is partially closing via a downward current flowing equatorward of the main auroral current system within the dawn sector, supported by increases in plasma intensity during compressions of Saturn's magnetosphere.

The upward auroral current region are the current of the main auroral current and map to ~13 R_s . This upward current is predominantly a combination of subcorotation currents and the PPO current system, as we shall see in the next section. It is clear that as tail reconnection occurs and hot plasma is injected from the tail towards Saturn, an enhanced upwards current is also associated with an increase in plasma intensity. We suggest that the plasma injected into the midnight-dawn sector during tail reconnection events results in an enhanced subcorotation current system.

5. Planetary Period Oscillations

In Figure 8 we further explore the relationship between the field-aligned current sheets and the northern, southern and beats phases of the PPO systems. In each panel the points are color-coded to show the magnetospheric conditions as used in earlier figures. Figure 8a-8c show the $I_{||}$ values for the downward current as functions of the northern, Ψ_N , southern, Ψ_S , and beat phases, Φ_B , respectively. Figure 8d-8e show the same for the upward current, $I_{||}$. The clearest observation here is that the upward current is significant modulated by the northern PPO system, being strongest at $\Psi_N \sim 90^\circ$ and weakest at $\Psi_N \sim 270^\circ$ (Figure 8d). This agrees with previous observations of the PPO-related current being upward directed at 90° and downward directed at 270° , therefore modulating the overall upward currents strength (Hunt et al., 2015, 2020). Interestingly, the largest current is observed when $\Psi_N \sim 90^\circ$ and the magnetosphere is compressed, showing that solar wind and magnetospheric conditions are also modulation the upward auroral current system.

The downward current region shown in Figure 8a-8c shows a less clear dependence on the PPO phases and more on the magnetospheric conditions with the compressed states (red, and orange) typically being higher than the normal (green) and expanded (blue) states. However, the PPO modulation of the downward current system is also evident. We would expect a peak downward directed PPO current at 270° . From Table 1 it is

clear that Rev 289 is the only event of which the downward northern PPO current system would contribute to the overall downward current sheet ($\Psi_N \sim 270^\circ$) (Hunt et al. 2015, 2020). From the information in Table 1 it is also clear that Rev 289 has the largest downward current I_{\parallel} observed within this dataset during a full compression case. Hunt et al., (2020) found that on average that for $\Psi_N = 270^\circ$ the total I_{\parallel} within the downward current sheet was ~ 0.9 MA/rad (see their Figure 7a). Therefore, considering this with the downward sheet values for the compression events implies the additional downward current is ~ 0.3 - 0.7 MA/rad in strength. This also broadly agrees with the difference in the I_{\parallel} values for the expanded/normal and compressed magnetospheric conditions.

6. Conclusions

In this paper we have examined the response of Saturn's northern hemisphere auroral field-aligned currents to magnetospheric conditions, specifically the compression state of the magnetosphere and the total ring current. We combined data from three studies, namely Hunt et al., (2020) for the properties of the northern hemisphere field-aligned currents, Bradley et al., (2020) for the magnetosphere compressions, and Provan et al., (2021) for the total ring current. We have focused on the downward currents flowing equatorward of the main auroral oval and the upward auroral currents of the main auroral oval.

Our key findings are:

1. The field-aligned currents respond to compressions of Saturn's magnetosphere. In particular, we found a clear relationship between the total current in the downward current sheet and compression events.
2. We found that for the cases with a stronger downward current there is also a stronger total ring current. Typically, these also corresponded to a compression event as identified by Bradley et al. (2020).
3. During magnetospheric compressions and tail reconnection events, the downward current region moves inwards towards Saturn.
4. The energetic particle intensities from the LEMMS instrument (E0-E2 and A1-A4) increased within the field regions carrying the upward and the downward currents for compression events. In particular, the higher energy protons (>255 keV) show the strongest response during a compression event, and these protons are likely to be from injected plasma due to nightside tail reconnection.

5. The upward auroral currents are also strengthened when the magnetosphere is compressed and tail reconnection occurs.

These observations support the suggestion that the nightside partial ring current reported by Provan et al., (2021) during the Grand Finale orbits closes via an additional strengthening of the downward current in the dawn sector. This additional current is approximately 0.5 MA/rad in strength, flowing equatorward of the main auroral upward current, and maps to the peak of the ring current. The additional downward current within Saturn's dawn sector is akin to Earth's Region 2 current, albeit having the opposite sense given the reversed polarity Saturn's core planetary field compared to Earth's field. These results show that Saturn's global current systems respond, partly, in a similar way to nightside reconnection and the resulting inflow of plasma as at Earth. Finally, we suggest that the plasma injected into the midnight-dawn sector during tail reconnection events results in an enhanced subcorotation current system resulting in an increase in the strength of the upward current.

Acknowledgements. Work at Imperial College was supported by UKRI/STFC grant ST/S000364/1. Work at the University of Leicester was supported by UKRI/STFC grant ST/N000749/1. T. J. B. was supported by STFC Quota Studentship ST/N504117/1. M. K. D. was funded by Royal Society Research Professorship RP140004. Calibrated magnetic field data and LEMMS from the Cassini mission are available from the NASA Planetary Data System (<https://pds-ppi.igpp.ucla.edu/search/?sc=Cassini&i=MAG>) and (<https://pds-ppi.igpp.ucla.edu/search/view/?f=yes&id=pds://PPI/CO-S-MIMI-4-LEMMS-CALIB-V1.0>). PPO phase data (2004-2017) are available from the University of Leicester Research Archive (<http://hdl.handle.net/2381/42436>). G.H would like to thank his co-authors, in particular, G.P and S.W.H.C for their help in completing the revisions as G.H is not long active in the research field.

References

- Alexeev, I. I., Kalegaev, V. V., Belenkaya, E. S., Bobrovnikov, S. Y., Bunce, E. J., Cowley, S. W. H., and Nichols, J. D. (2006), A global magnetic model of Saturn's magnetosphere and a comparison with Cassini SOI data, *Geophys. Res. Lett.*, 33, L08101, doi:10.1029/2006GL025896.
- Armstrong, T. P., Taherion, S., Manweiler, J., Krimigis, S., Paranicas, C., Mitchell, D., & Krupp, N. (2009). Energetic ions trapped in Saturn's inner magnetosphere. *Planetary and Space Science*, 57, 1723–1731. <https://doi.org/10.1016/j.pss.2009.03.008>
- Bradley, T. J., Cowley, S. W. H., Provan, G., Hunt, G. J., Bunce, E. J., Wharton, S. J., et al. (2018). Field-Aligned Currents in Saturn's Nightside Magnetosphere: Subcorotation and Planetary Period Oscillation Components During Northern Spring. *Journal of Geophysical Research: Space Physics*, 123(5), 3602–3636. <https://doi.org/10.1029/2017JA024885>
- Bradley, T. J., Cowley, S. W. H., Bunce, E. J., Melin, H., Provan, G., & Nichols, J. D., et al. (2020). Saturn's nightside dynamics during Cassini's F ring and proximal orbits: Response to solar wind and planetary period oscillation modulations. *Journal of Geophysical Research: Space Physics*, 125, e2020JA027907. <https://doi.org/10.1029/2020JA027907>
- Bunce, E. J., Cowley, S. W. H., Alexeev, I. I., Arridge, C. S., Dougherty, M. K., Nichols, J. D., & Russell, C. T. (2007). Cassini observations of the variation of Saturn's ring current parameters with system size. *Journal of Geophysical Research*, 112(A10), A10202. <https://doi.org/10.1029/2007JA012275>
- Bunce, E. J., Arridge, C. S., Clarke, J. T., Coates, A. J., Cowley, S. W. H., Dougherty, M. K., et al. (2008). Origin of Saturn's aurora: Simultaneous observations by Cassini and the Hubble Space Telescope. *Journal of Geophysical Research*, 113(A9), A09209. <https://doi.org/10.1029/2008JA013257>
- Carbary, J. F. (2012). The morphology of Saturn's ultraviolet aurora. *Journal of Geophysical Research*, 117(A6), A06210. <https://doi.org/10.1029/2012JA017670>
- Carbary, J. F. (2019). A new ring current model for Saturn. *Journal of Geophysical Research: Space Physics*, 124, 3378–3389. <https://doi.org/10.1029/2019JA026560>
- Carbary, J. F., and Mitchell, D. G. (2013). Periodicities in Saturn's magnetosphere, *Rev. Geophys.*, 51, 1–30, doi:10.1002/rog.20006.
- Connerney, J. E. P., Acuña, M. H., & Ness, N. F. (1981). Saturn's ring current and inner magnetosphere. *Nature*, 292, 724–726.
- Connerney, J. E. P., Acuña, M. H., & Ness, N. F. (1983). Currents in Saturn's magnetosphere. *Journal of Geophysical Research*, 88, 8779–8789.
- Cowley, S. W. H. (2000), Magnetosphere-ionosphere interactions: A tutorial review, in *Magnetospheric Current Systems, Geophys. Monogr. Ser.*, vol. 118, pp. 91–106, AGU, Washington, D. C.
- Cowley, S. W. H., Badman, S. V., Bunce, E. J., Clarke, J. T., Gérard, J.-C., Grodent, D., et al. (2005).

- Reconnection in a rotation-dominated magnetosphere and its relation to Saturn's auroral dynamics. *Journal of Geophysical Research*, 110, A02201. <https://doi.org/10.1029/2004JA010796>
- Cowley, S. W. H., Bunce, E. J., & Prangé, R. (2004). Saturn's polar ionospheric flows and their relation to the main auroral oval. *Annales Geophysicae*, 22, 1379–1394.
- Cowley, S. W. H., Arridge, C. S., Bunce, E. J., Clarke, J. T., Coates, A. J., Dougherty, M. K., et al. (2008). Auroral current systems in Saturn's magnetosphere: comparison of theoretical models with Cassini and HST observations. *Annales Geophysicae*, 26(9), 2613–2630. <https://doi.org/10.5194/angeo-26-2613-2008>
- Coxon, J. C., Milan, S. E., Clausen, L. B. N., Anderson, B. J., and Korth, H. (2015), The magnitudes of the regions 1 and 2 Birkeland currents observed by AMPERE and their role in solar wind-magnetosphere-ionosphere coupling, *J. Geophys. Res. Space Physics*, 119, 9804–9815, doi:10.1002/2014JA020138.
- Dougherty, M. K., Kellock, S., Southwood, D. J., Balogh, A., Smith, E. J., Tsurutani, B. T., et al. (2004). The Cassini Magnetic Field Investigation. *Space Science Reviews*, 114(1–4), 331–383. <https://doi.org/10.1007/s11214-004-1432-2>
- Hunt, G. J., Cowley, S. W. H., Provan, G., Bunce, E. J., Alexeev, I. I., Belenkaya, E. S., et al. (2014). Field-aligned currents in Saturn's southern nightside magnetosphere: Subcorotation and planetary period oscillation components. *Journal of Geophysical Research A: Space Physics*, 119(12), 9847–9899. <https://doi.org/10.1002/2014JA020506>
- Hunt, G. J., Cowley, S. W. H., Provan, G., Bunce, E. J., Alexeev, I. I., Belenkaya, E. S., et al. (2015). Field-aligned currents in Saturn's northern nightside magnetosphere: Evidence for interhemispheric current flow associated with planetary period oscillations. *Journal of Geophysical Research: Space Physics*, 120(9), 7552–7584. <https://doi.org/10.1002/2015JA021454>
- Hunt, G. J., Cowley, S. W. H., Provan, G., Bunce, E. J., Alexeev, I. I., Belenkaya, E. S., et al. (2016). Field-aligned currents in Saturn's magnetosphere: Local time dependence of southern summer currents in the dawn sector between midnight and noon. *Journal of Geophysical Research: Space Physics*, 121(8), 7785–7804. <https://doi.org/10.1002/2016JA022712>
- Hunt, G. J., Provan, G., Bunce, E. J., Cowley, S. W. H., Dougherty, M. K., & Southwood, D. J. (2018). Field-Aligned Currents in Saturn's Magnetosphere: Observations From the F-Ring Orbits. *Journal of Geophysical Research: Space Physics*, 123(5), 3806–3821. <https://doi.org/10.1029/2017JA025067>
- Hunt, G. J., Bunce, E. J., Cao, H., Cowley, S. W. H., Dougherty, M. K., Provan, G., & Southwood, D. J. (2020). Saturn's auroral field-aligned currents: Observations from the northern hemisphere dawn sector during Cassini's proximal orbits. *Journal of Geophysical Research: Space Physics*, 125, e2019JA027683. <https://doi.org/10.1029/2019JA027683>
- Kanani, S. J., Arridge, C. S., Jones, G. H., Fazakerley, A. N., McAndrews, H. J., Sergis, N., et al. (2010). A new form of Saturn's magnetopause using a dynamic pressure balance model, based on in situ, multi-

- instrument Cassini measurements. *Journal of Geophysical Research*, 115, A06207.
<https://doi.org/10.1029/2009JA014262>
- Kellett, S., Arridge, C. S., Bunce, E. J., Coates, A. J., Cowley, S. W. H., Dougherty, M. K., Persoon, A. M., Sergis, N., and Wilson, R. J. (2011), Saturn's ring current: Local time dependence and temporal variability, *J. Geophys. Res.*, 116, A05220, doi:10.1029/2010JA016216.
- Khurana, K. K. (2001), Influence of solar wind on Jupiter's magnetosphere deduced from currents in the equatorial plane, *J. Geophys. Res.*, 106, 25999–26016, doi:10.1029/2000JA000352.
- Kinrade, J., Badman, S. V., Paranicas, C., Mitchell, D. G., Arridge, C. S., Gray, R. L., et al. (2020). Tracking counterpart signatures in Saturn's auroras and ENAimagery during large-scale plasmainjection events. *Journal of Geophysical Research: Space Physics*, 125, e2019JA027542.
<https://doi.org/10.1029/2019JA027542>
- Krimigis, S. M., Mitchell, D. G., Hamilton, D. C., Livi, S., Dandouras, J., Jaskulek, S., et al. (2004). Magnetosphere Imaging Instrument (MIMI) on the Cassini Mission to Saturn/Titan. *Space Science Reviews*, 114, 233–329. <https://doi.org/10.1029/10.1007/s11214-004-1410-8>
- Lorch, C. T. S., Ray, L. C., Arridge, C. S., Khurana, K. K., Martin, C. J., & Bader, A. (2020). Local time asymmetries in Jupiter's magnetodisc currents. *Journal of Geophysical Research: Space Physics*, 125, e2019JA027455. <https://doi.org/10.1029/2019JA027455>
- Martin, C. J., & Arridge, C. S. (2019). Current density in Saturn's equatorial current sheet: Cassini magnetometer observations. *Journal Geophysical Researcher: Space Physics*, 124, 279–292.
<https://doi.org/10.1029/2018JA025970>
- Mitchell, D. G., Krimigis, S. M., Paranicas, C. P., Brandt, P. C., Carbary, J. F., Roelof, E. C., et al. (2009). Recurrent energization of plasma in the midnight-to-dawn quadrant of Saturn's magnetosphere, and its relationship ion to auroral UV and radio. *Planetary and Space Science*, 57,1732–1742.
<https://doi.org/10.1016/j.pss.2009.04.002>
- Provan, G., Cowley, S. W. H., Bradley, T. J., Bunce, E. J., Hunt, G. J., & Dougherty, M. K. (2018). Planetary period oscillations in Saturn's magnetosphere: Cassini magnetic field observations over the northern summer solstice interval. *Journal of Geophysical Research: Space Physics*, 123, 3859–3899.
<https://doi.org/10.1029/2018JA025237>
- Provan, G., Bradley, T. J., Bunce, E. J., Cowley, S. W. H., Cao, H., Dougherty, M., et al. (2021). Saturn's nightside ring current during Cassini's Grand Finale. *Journal of Geophysical Research: Space Physics*, 126, e2020JA028605. <https://doi.org/10.1029/2020JA028605>
- Roussos, E., Jackman, C. M., Thomsen, M. F., Kurth, W. S., Badman, S. V., Paranicas, C., et al. (2018). Solar energetic particles (SEP) and galactic cosmic rays (GCR) as tracers of solar wind conditions near Saturn: Event lists and applications. *Icarus*, 300, 47–71. <https://doi.org/10.1016/j.icarus.2017.08.040>
- Roussos, E., Krupp, N., Paranicas, C., Kollmann, P., Mitchell, D. G., Krimigis, S. M., et al. (2018).

- 546 Heliospheric conditions at Saturn during Cassini's ring grazing and proximal orbits. *Geophysical*
 547 *Research Letters*, 45, 10812–10818. <https://doi.org/10.1029/2018GL078093>
- 548 Schippers, P., et al. (2008), Multi-instrument analysis of electron populations in Saturn's magnetosphere, *J.*
 549 *Geophys. Res.*, 113, A07208, doi:10.1029/2008JA013098.
- 550 Sergis, N., C. M. Jackman, M. F. Thomsen, S. M. Krimigis, D. G. Mitchell, D. C. Hamilton, M. K.
 551 Dougherty, N. Krupp, and R. J. Wilson (2017), Radial and local time structure of the Saturnian
 552 ring current, revealed by Cassini, *J. Geophys. Res. Space Physics*, 122, 1803–
 553 1815, doi:10.1002/2016JA023742.
- 554 Sittler, E. C. N. Andre, M. Blanc, M. Burger, R. E. Johnson, A. Coates, A. Rymer, D. Reisenfeld, M. F.
 555 Thomsen, A. Persoon, M. Dougherty, H. T. Smith, R. A. Baragiola, R. E. Hartle, D. Chornay, M. D.
 556 Shappirio, D. Simpson, D. J. McComas, D. T. Young (2008). Ion and neutral sources and sinks within
 557 Saturn's inner magnetosphere: Cassini results, *Planetary and Space Science*, 56, 3-18,
 558 <https://doi.org/10.1016/j.pss.2007.06.006>
- 559 Southwood, D. J., & Cowley, S. W. H. (2014). The origin of Saturn's magnetic periodicities: Northern and
 560 southern current systems. *Journal of Geophysical Research: Space Physics*, 119(3), 1563–1571.
 561 <https://doi.org/10.1002/2013JA019632>
- 562 Southwood, D. J., & Kivelson, M. G. (2007). Saturnian magnetospheric dynamics: Elucidation of a camshaft
 563 model. *Journal of Geophysical Research*, 112(A12), A12222. <https://doi.org/10.1029/2007JA012254>
- 564 Talboys, D. L., Arridge, C. S., Bunce, E. J., Coates, A. J., Cowley, S. W. H., & Dougherty, M. K. (2009).
 565 Characterization of auroral current systems in Saturn's magnetosphere: High-latitude Cassini
 566 observations. *Journal of Geophysical Research*, 114(A6), A06220.
 567 <https://doi.org/10.1029/2008JA013846>
- 568 Talboys, D. L., Arridge, C. S., Bunce, E. J., Coates, A. J., Cowley, S. W. H., Dougherty, M. K., & Khurana,
 569 K. K. (2009). Signatures of field-aligned currents in Saturn's nightside magnetosphere. *Geophysical*
 570 *Research Letters*, 36(19), L19107. <https://doi.org/10.1029/2009GL039867>
- 571 Talboys, D. L., Bunce, E. J., Cowley, S. W. H., Arridge, C. S., Coates, A. J., & Dougherty, M. K. (2011).
 572 Statistical characteristics of field-aligned currents in Saturn's nightside magnetosphere. *Journal of*
 573 *Geophysical Research*, 116(A4), A04213. <https://doi.org/10.1029/2010JA016102>
- 574 Tao, C., Kataoka, R., Fukunishi, H., Takahashi, Y., & Yokoyama, T. (2005). Magnetic field variations in the
 575 Jovian magnetotail induced by solar wind dynamic pressure enhancements. *Journal of Geophysical*
 576 *Research*, 110, A11208. <https://doi.org/10.1029/2004JA010959>
- 577 Thomsen, M. F., & Coates, A. J. (2019). Saturn's plasmopause: Signature of magnetospheric dynamics.
 578 *Journal of Geophysical Research: Space Physics*, 124, 8804– 8813.
 579 <https://doi.org/10.1029/2019JA027075>
- 580 Zieger, B., & Hansen, K. C. (2008). Statistical validation of a solar wind propagation model from 1 to 10

581 AU. *Journal of Geophysical Research*, 113, A08107. <https://doi.org/10.1029/2008JA013046>

582

583 **Table 1.** Field-aligned current sheets boundary times and properties from Hunt et al. (2020) as shown in Figures 3, 4, and 5.

Rev	Boundary 2 time Day/Month Hour:Min (Year 2017)	Boundary 3 time Day/Month Hour:Min (Year 2017)	Boundary 4 time Day/Month Hour:Min (Year 2017)	Upward sheet current I_{\parallel} /MA/rad	Downward sheet current I_{\parallel} /MA/rad	Upward sheet position θ_{iN} /°	Downward sheet position θ_{iN} /°	Equatorial radial distanced of upward current sheet /Rs	Equatorial radial distance of downward current sheet /Rs	IT /MA	Rm /Rs	Magnetospheric State
271	26/04 07:07	26/04 07:40	26/04 07:43	2.457	0.887	15.783	16.782	14.51	11.68	14.32	29.98	Normal
273	09/05 04:43	09/05 04:53	09/05 04:58	2.140	0.709	16.066	16.805	13.63	11.62	16.87	35.02	Normal
274	15/05 14:45	15/05 15:17	15/05 15:28	2.817	1.212	15.513	16.701	15.34	11.91	18.53	20.53	Compressed
275	22/05 01:27	22/05 01:52	22/05 02:03	1.109	0.467	15.900	17.599	14.15	9.78	18.08	23.34	Expanded
276	28/05 12:24	28/05 13:05	28/05 13:18	1.682	0.858	16.036	18.426	13.72	8.37	15.81	21.41	Compressed
278	10/06 11:11	10/06 11:35	10/06 11:42	0.707	0.727	16.436	18.216	12.5	8.69	15.75	29.62	Normal
279	16/06 22:04	16/06 22:34	16/06 22:50	2.554	1.003	16.001	18.625	13.83	8.09	15.27	27.36	Normal
281	29/06 20:25	29/06 21:04	29/06 21:05	1.196	0.564	17.182	19.386	10.54	7.19	17.01	27.95	Expanded
282	06/07 07:50	06/07 08:07	06/07 08:17	2.046	0.837	15.847	17.071	14.31	10.94	15.89	26.36	Expanded
283	12/07 18:38	12/07 19:18	12/07 19:34	1.817	1.048	15.595	17.339	15.09	10.32	15.24	25.4	Normal
284	19/07 06:24	19/07 06:30	19/07 06:36	2.269	0.588	16.440	17.152	12.49	10.75	15.92	26.07	Normal
285	25/07 17:15	25/07 17:34	25/07 17:42	3.135	1.824	16.023	17.266	13.76	10.48	16.58	22.20	Part Compressed
286	01/08 04:36	01/08 04:44	01/08 04:57	1.401	0.738	16.382	17.877	12.66	9.26	15.31	22.17	Expanded
287	07/08 15:52	07/08 16:05	07/08 16:09	1.957	0.590	16.938	18.055	11.13	8.95	17.38	24.21	Normal
288	14/08 02:26	14/08 03:00	14/08 03:21	1.973	1.008	16.049	19.255	13.68	7.33	20.48	20.57	Compressed
289	20/08 13:53	20/08 14:00	20/08 14:15	2.808	1.586	16.679	18.341	11.81	8.50	21.77	19.36	Compressed
290	27/08 00:37	27/08 00:57	27/08 01:19	2.057	0.699	16.394	19.881	12.63	6.70	16.68	32.78	Expanded
291	02/09 11:02	02/09 11:43	02/09 11:57	2.290	1.524	15.622	17.165	15.01	10.72	16.55	21.04	Normal
292	08/09 22:16	08/09 22:56	08/09 23:12	1.781	0.738	16.890	20.970	11.25	5.880	17.81	21.32	Part compressed

Figure Captions

Figure 1. Sketches of northern hemisphere field-aligned currents and the proposed partial nightside ring current system proposed by Provan et al. (2021) which is not to scale. (a) Projected of the northern non-PPO and PPO currents into the northern ionosphere as viewed from above. The light blue circle in the polar region depicts the non-PPO downward subcorotation currents, the pink circle shows the non-PPO upwards subcorotation currents of the main auroral oval. The green circled crossed and dots show the downward and upward field-aligned currents, respectively. The green arrowed lines show the ionospheric closure current (I_m). The darker blue arrowed lines shown the magnetic field perturbations associated with the northern PPO system mapped to the ionosphere. The red twin vortex shows the expected atmospheric flows associated with the PPOs. Dashed centered circle indicates the open-closed boundary (OCB). The key northern PPO phases are shown around the edge. (b) Magnetospheric view of the current systems as viewed from the nightside during normal magnetospheric conditions showing the 90°-270° PPO meridian. Saturn's magnetospheric ring current is shown by the grey ring, the direction and total current (I_T) are shown. (c) The same view as (b) but for compressed magnetospheric conditions, the proposed partial ring current and associated closures currents are shown by the red arrows.

Figure 2. Cassini trajectories plotted in the $\rho - z$ plane panel (a), and mapped to the northern ionosphere, panel (b). (a) A typical Cassini Rev from the proximal orbits, namely Rev 273. Day of year markers (2017) are shown with the smaller black circles marking every 3 hours. The magnetic field lines are determined from a model comprising of a 3-degree planetary magnetic field plus ring current (see text). The grey shaded region shows the typical magnetic field region where the auroral field-aligned currents flow. (b) Comparison between northern hemisphere ionospheric projections of two proximal orbits, Rev 273 (blue) and Rev 289 (red), using the same magnetic field as shown in (a). The DOY:hh label are shown. Statistical auroral boundaries (solid lines) as defined by the peak and half power emission points (shown by the center line with crosses and the solid lines respectively) determined from Cassini Ultraviolet Imaging Spectrograph observations (Carbary, 2012).

Figure 3. Comparison of northern in-situ observations from Rev 273 (panels a-d) and Rev 289 (panels e-h), these being normal and compressed magnetosphere cases, respectively according to Bradley et al., (2020). Panels (a) and (d) show the ionospheric meridional current at the feet of the field lines, I_m (MA/rad),

613 determined from the azimuthal magnetic field measured by the Cassini spacecraft. Panels (b) and (f) show
 614 the electron intensities from Cassini LEMMS electron channels E0-E2 110-1350 keV ($1/\text{cm}^2 \text{ sr s keV}$),
 615 color-coded as in the figure. Panels (c) and (g) show the proton intensities from Cassini LEMMS electron
 616 channels A1-A4 35-506 keV ($1/\text{cm}^2 \text{ sr s keV}$), color-coded as shown in the figure. Panels (d) and (h) show
 617 the ionospheric colatitude of Cassini's magnetically mapped footprint in the northern hemisphere. The
 618 mapping is the same as used on the Figure 1b. The vertical dashed lines mark the boundaries of the main
 619 upward (auroral) and downward field-aligned current sheets as determined by Hunt et al. (2020) from
 620 gradients in I_m .

621 **Figure 4.** Panel (a) presents the total ring current current (I_T) from Provan et al. (2021), determined on a rev-
 622 by-rev basis. Panel (b) presents the downward field-aligned current (I_{\parallel}) and Panel (c) the ionospheric
 623 colatitude of the center of the downward field-aligned current region (θ_{IN}). Panel (d) shows the upward
 624 field-aligned current (I_{\parallel}) and Panel (e) the ionospheric colatitude of the center of the upward field-aligned
 625 current region (data for Panels b-e from Hunt et al. (2020)). The data in each panel is plotted versus subsolar
 626 magnetopause stand-off distance, R_M , determined using the model of Kanani et al. (2010) Each point is
 627 color-coded according to the magnetospheric compression state determined by Bradley et al., (2020) with the
 628 color-code presented on the figure.

629 **Figure 5.** Comparison of the current within the field-aligned current sheets (I_{\parallel}) with the total ring current for
 630 that Rev determined by Provan et al (2021) (I_T). Panel (a) shows downward field-aligned current while panel
 631 (b) shows the upward field-aligned current. Each point is color-coded according to the magnetospheric
 632 compression state determined by Bradley et al., (2020) as shown in the figure legend. The larger circles show
 633 the mean values. The mean value are for a compressed magnetosphere (large red circle), compressed and
 634 partially-compressed magnetosphere (large red circle with an orange center), expanded magnetosphere
 635 (large blue circle) and for when the magnetosphere is in a normal or expanded state (large blue circle with a
 636 green center).

637 **Figure 6.** Average energetic electron and proton intensities within the downward (panels a-d) and upward
 638 (panels e-h) field-aligned current sheet region for Revs 271-292, together with the northern and southern
 639 PPO phases, northern ionospheric colatitude, and mapped equatorial radial distance of the center of the
 640 current sheet. (a and e) Average electron E0-E2 (110-1350 keV) LEMMS intensities color-coded as shown

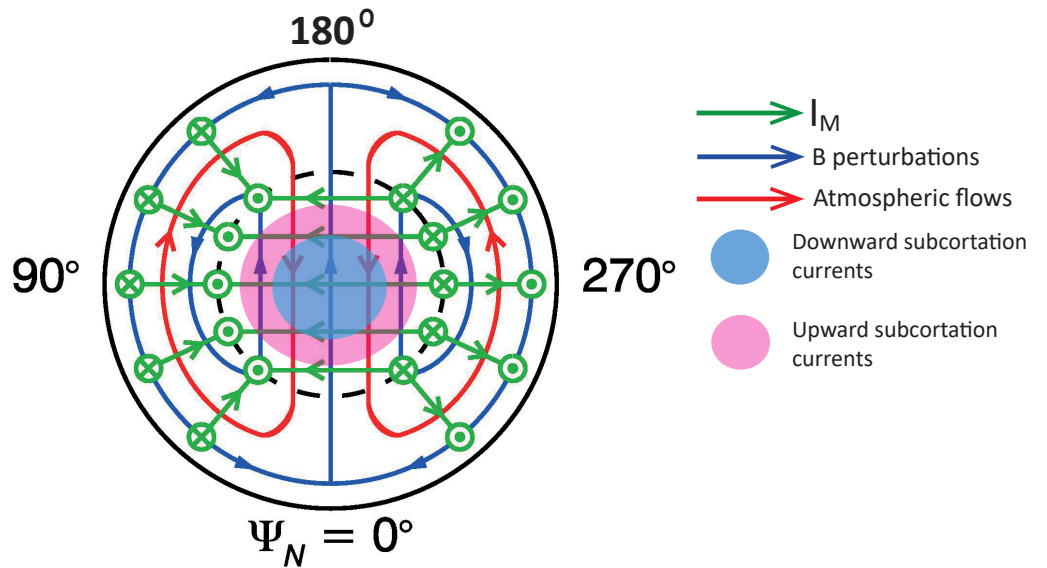
in the figure. (b and f) Average proton A1-A4 (35-506 keV) LEMMS intensities color-coded as shown in the figure. (c and g) Magnetically mapped northern hemisphere ionospheric colatitude (black) and the corresponding equatorial radial distance of the field line (red dashed line). (d and h) Northern, Southern and Beat PPO phases, shown by the blue and red circle, and black crosses, respectively. Vertical red lines show the compression event Revs, whilst the orange lines show the partial compression Revs. The horizontal orange bar marks when the PPO phases are between 90° - 270° .

Figure 7. Average energetic electron E0-E2 LEMMS (panels a and c) and protons A1-A4 LEMMS (panels b and d) intensity within the downward (panels a and b) and upward (panels c and d) field-aligned current sheet regions for Revs 271-297, plotted versus the total ring current current I_T as determined by Provan et al. (2021). The intensities are shown as circles where the outer edge shows is color coded by energy channel as shown in the figure, using the same color scale as in Figure 6. The center of the circles are color coded by magnetospheric compression state as shown in the figure.

Figure 8. Downward field-aligned current plotted versus northern PPO phase Ψ_N (panel a), southern PPO phase Ψ_S (pane b) and beat phases, Φ_B (panel c). Panels d-f show the same for the upward field-aligned current ($I_{||}$). The circles are color coded by magnetospheric compression state as shown in the figure.

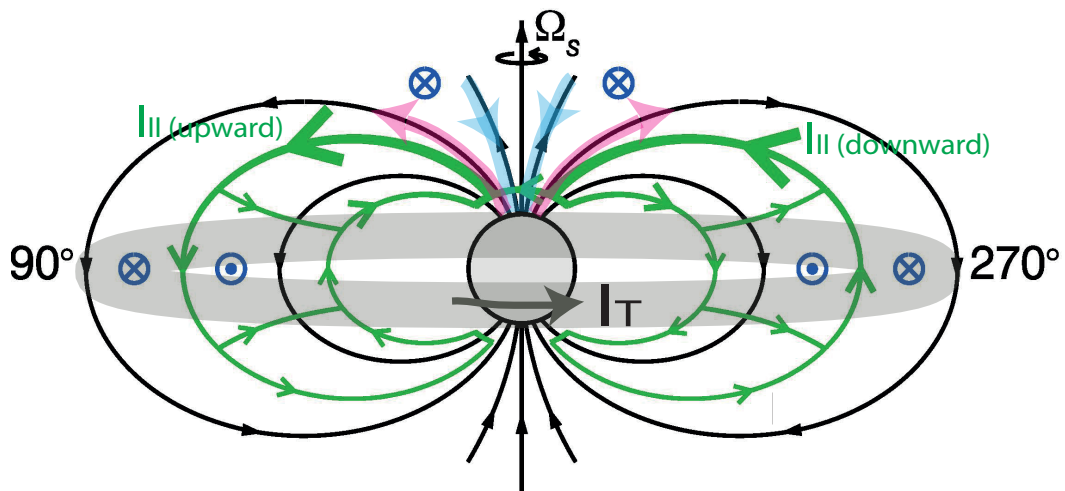
Figure 1.

(a)



Normal magnetospheric conditions

(b)



Compressed magnetospheric conditions

(c)

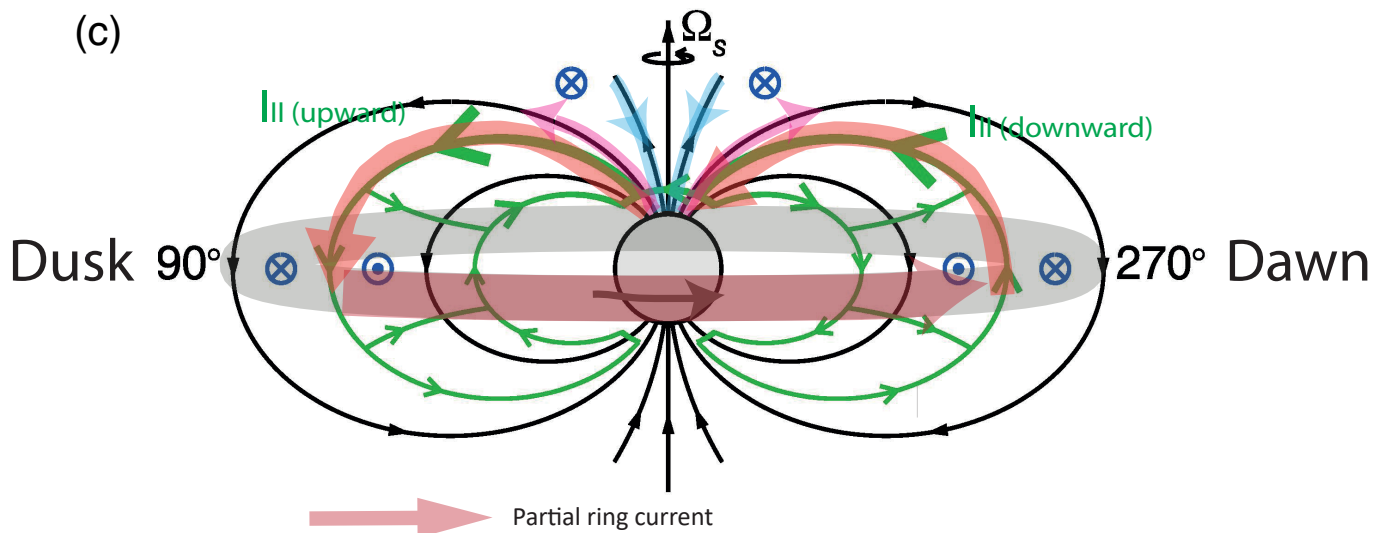


Figure 2.

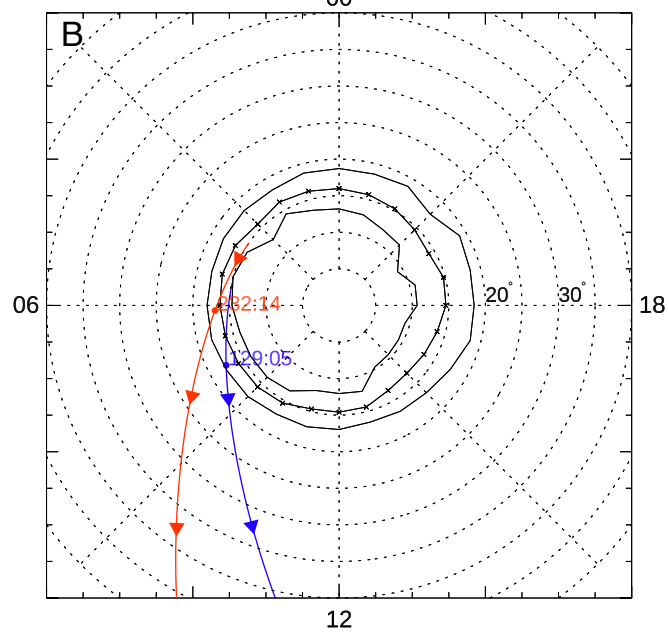
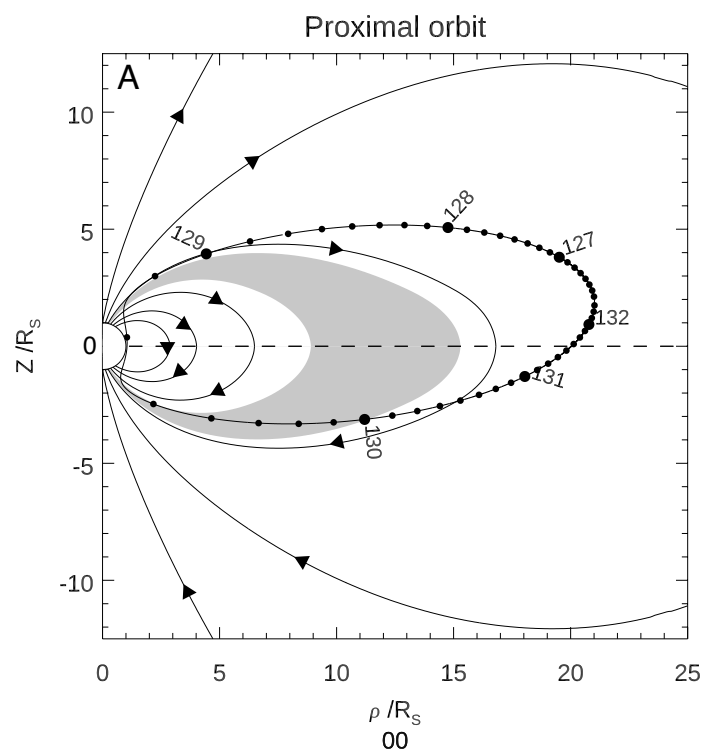


Figure 3.

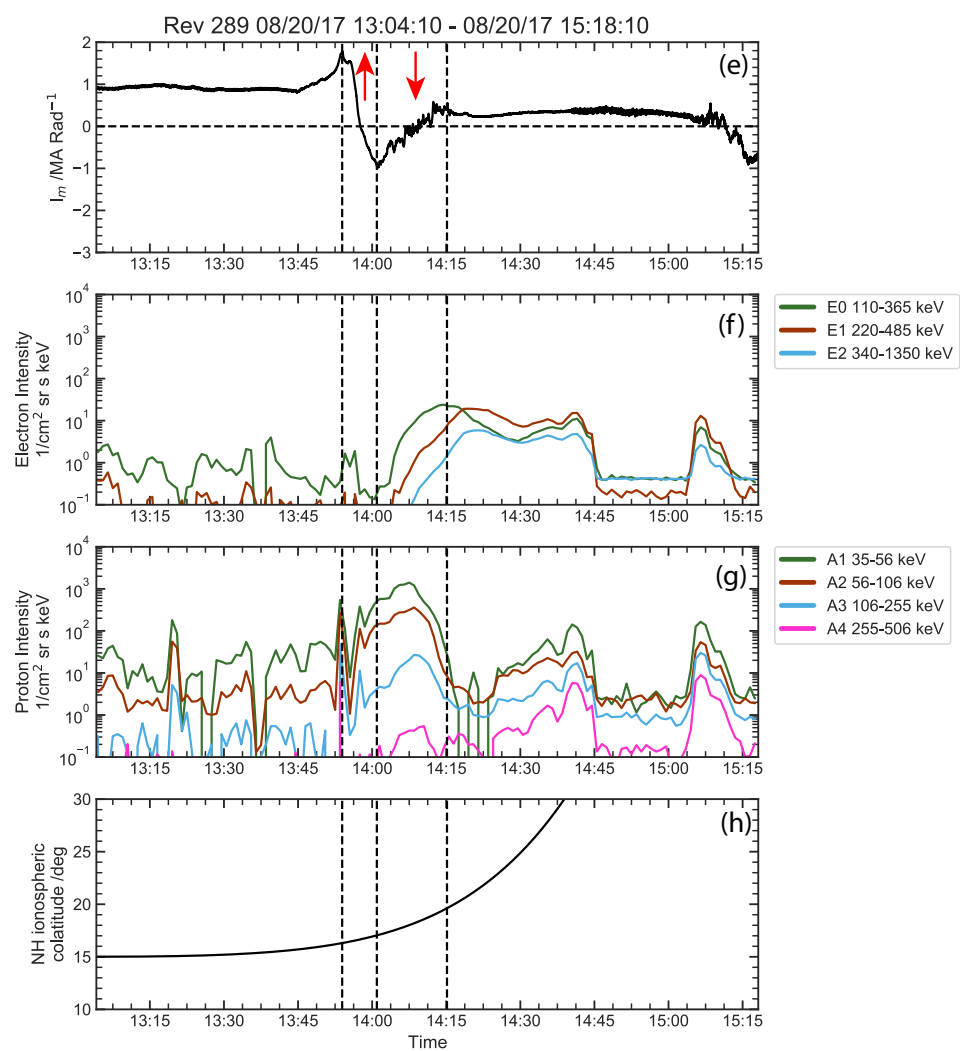
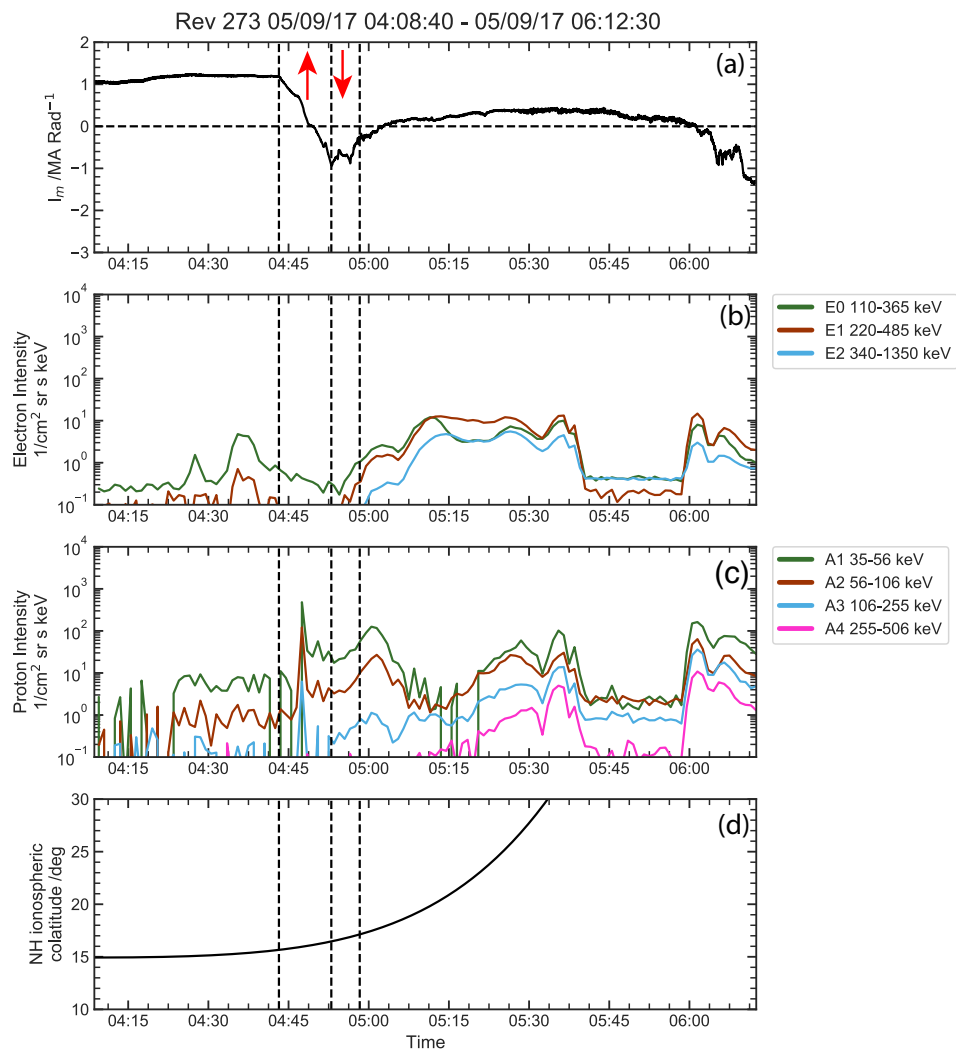


Figure 4.

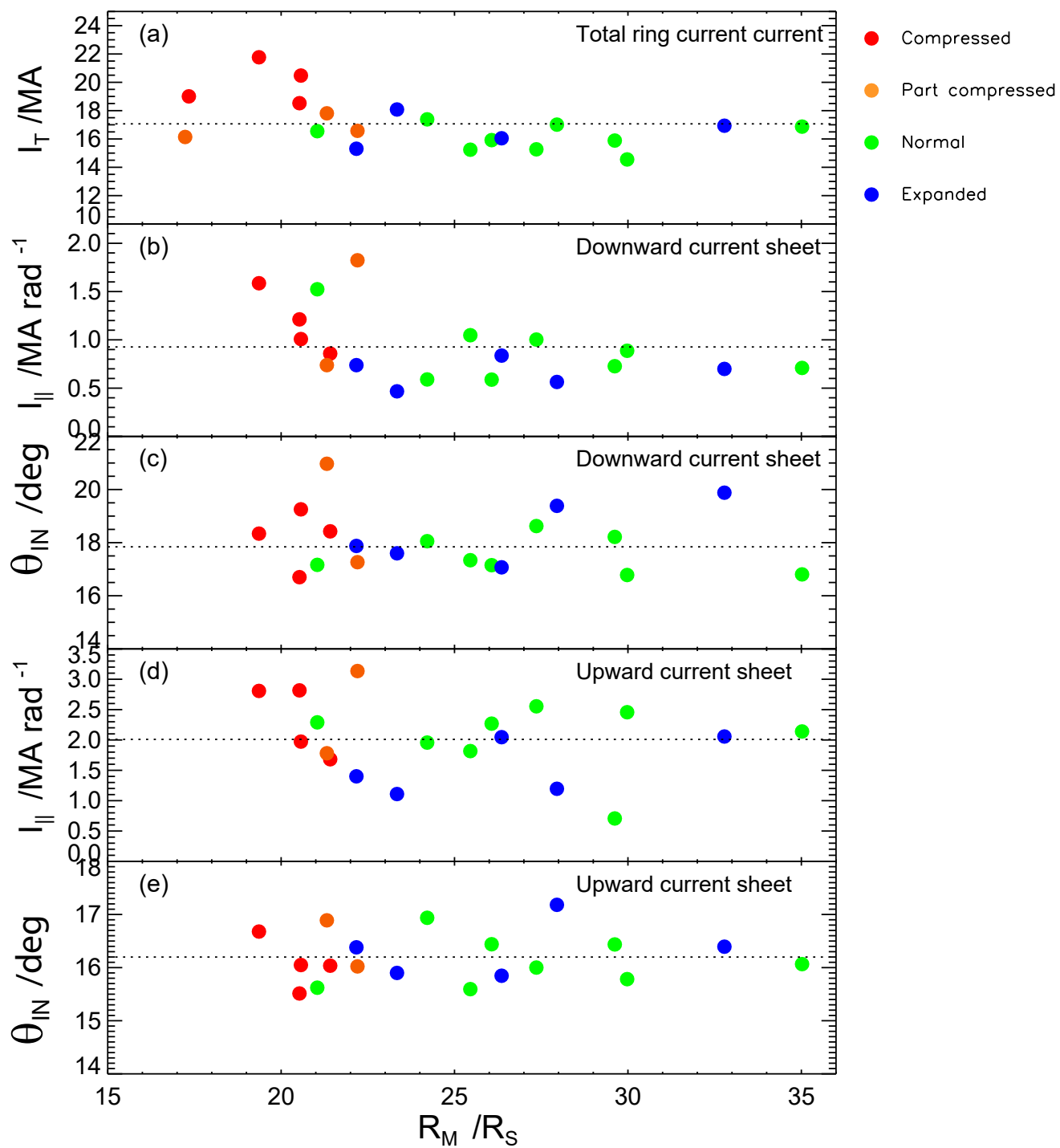


Figure 5.

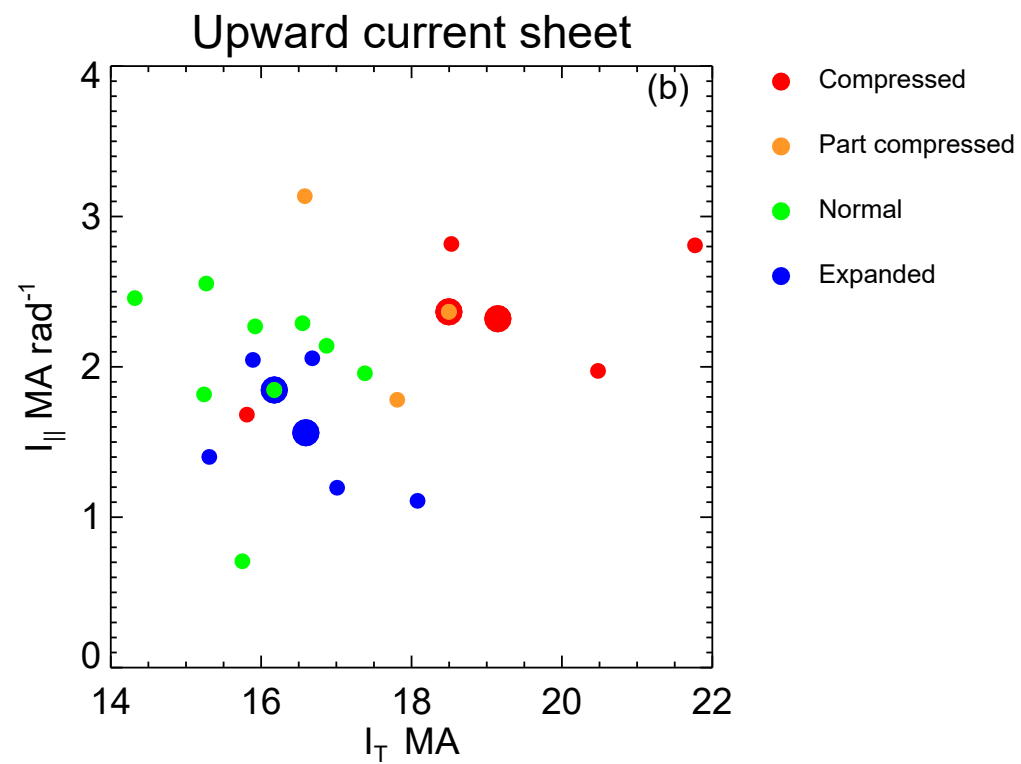
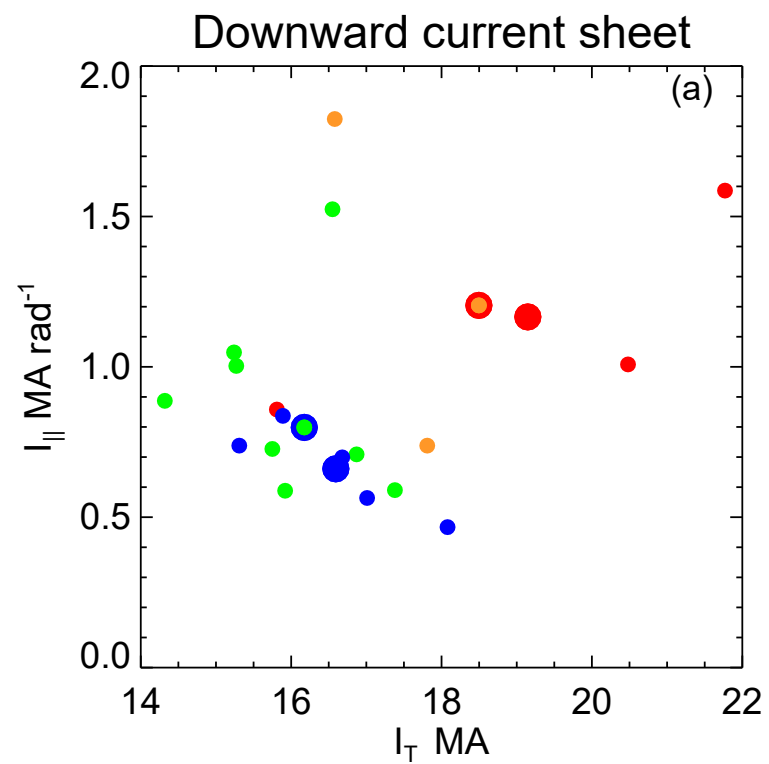


Figure 6.

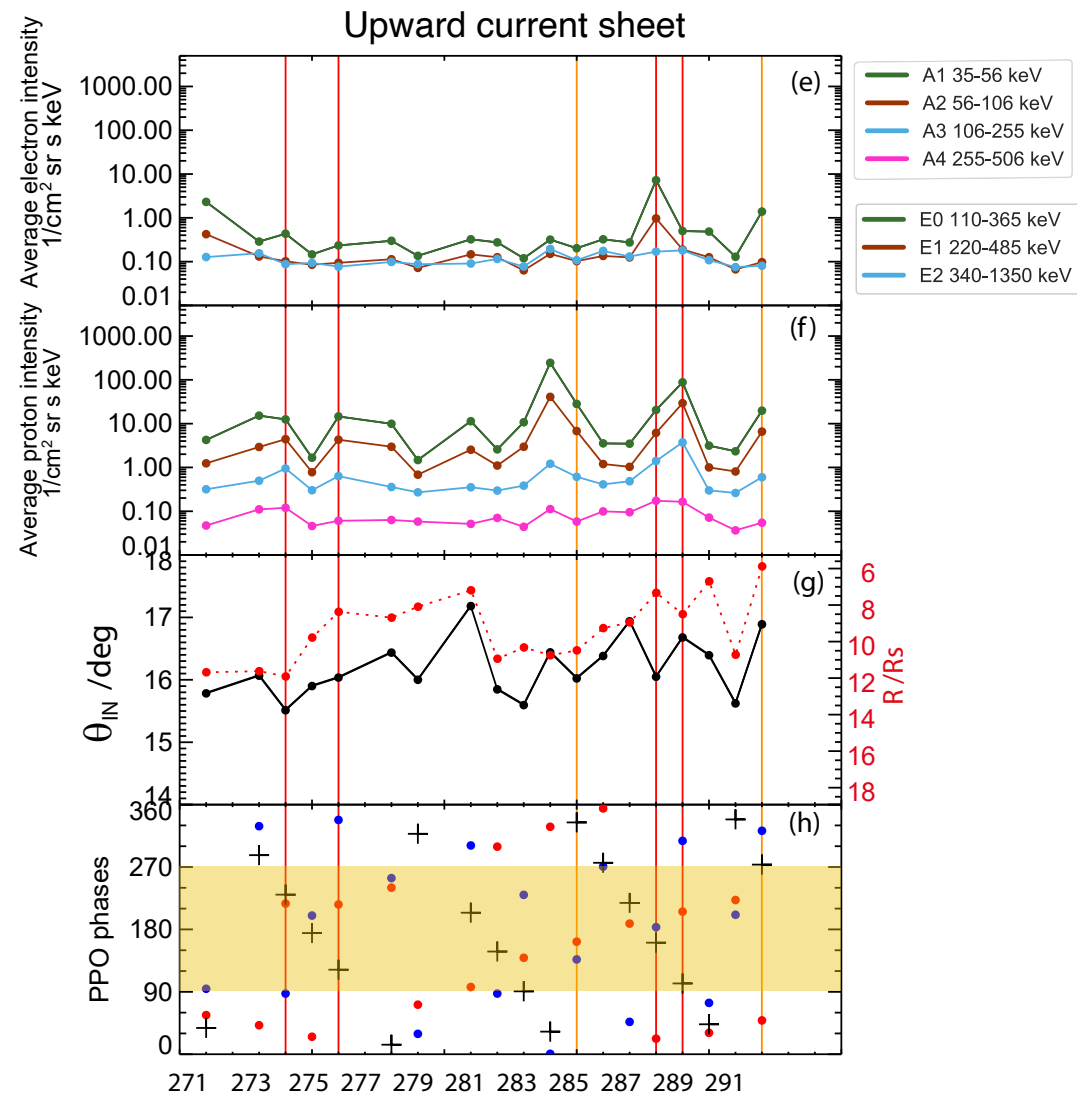
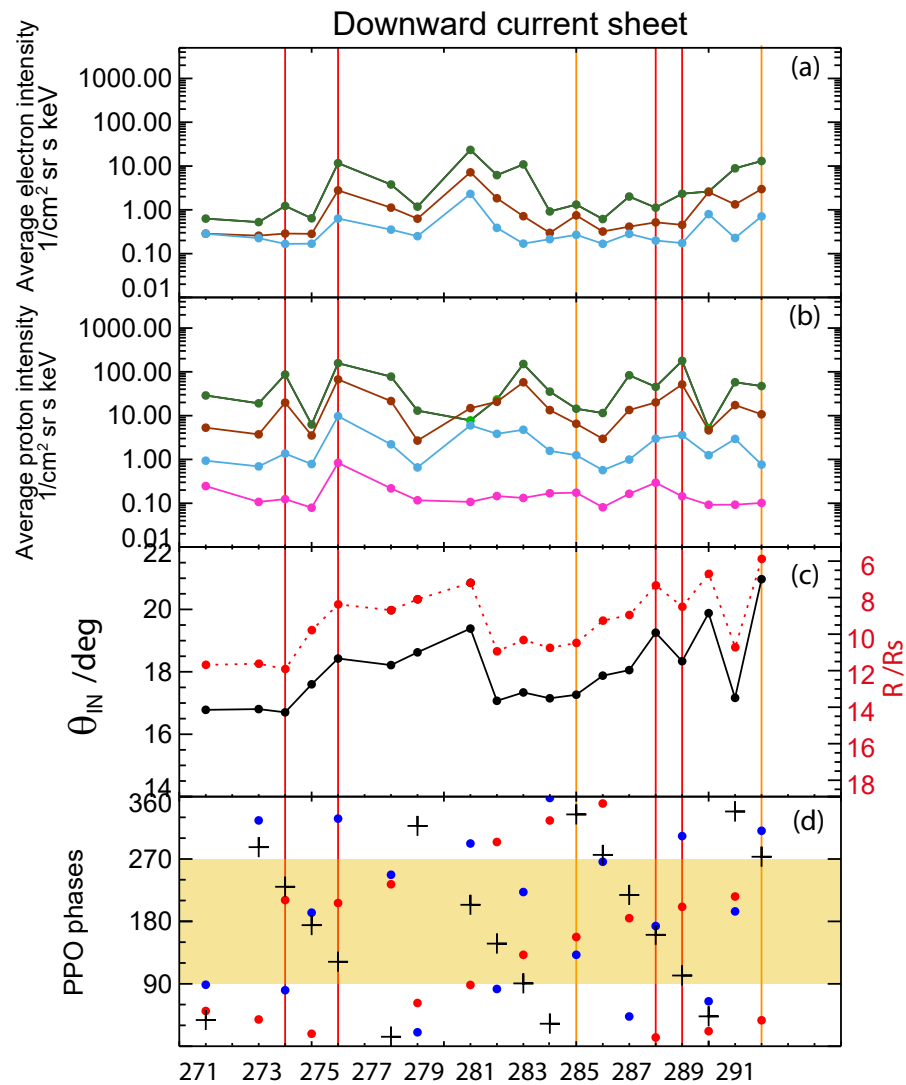
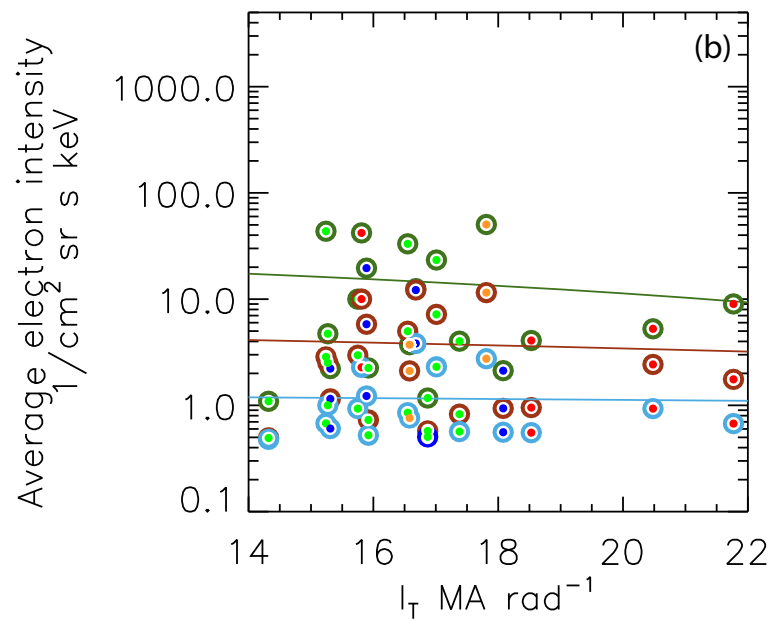
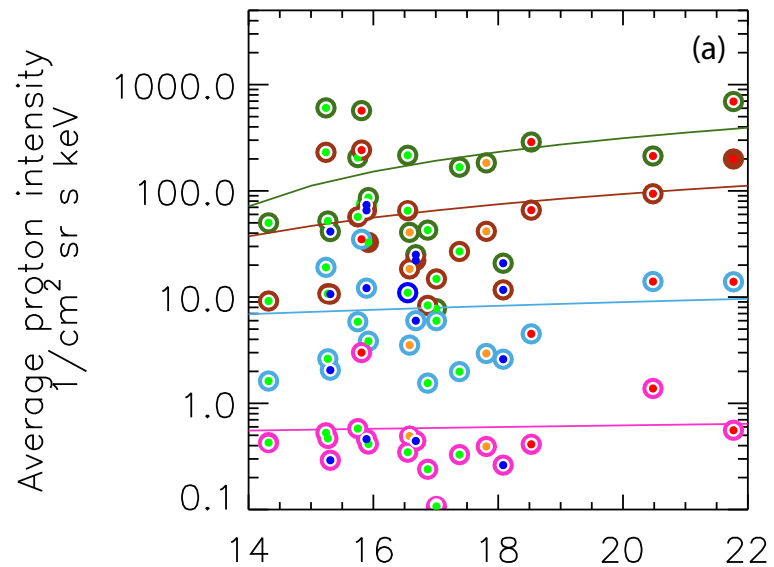


Figure 7.

Downward current sheet



Upward current sheet

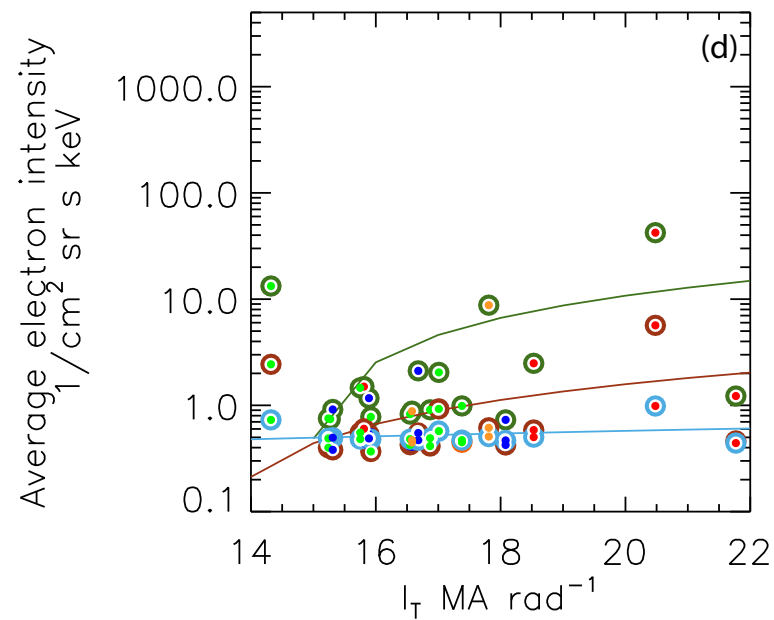
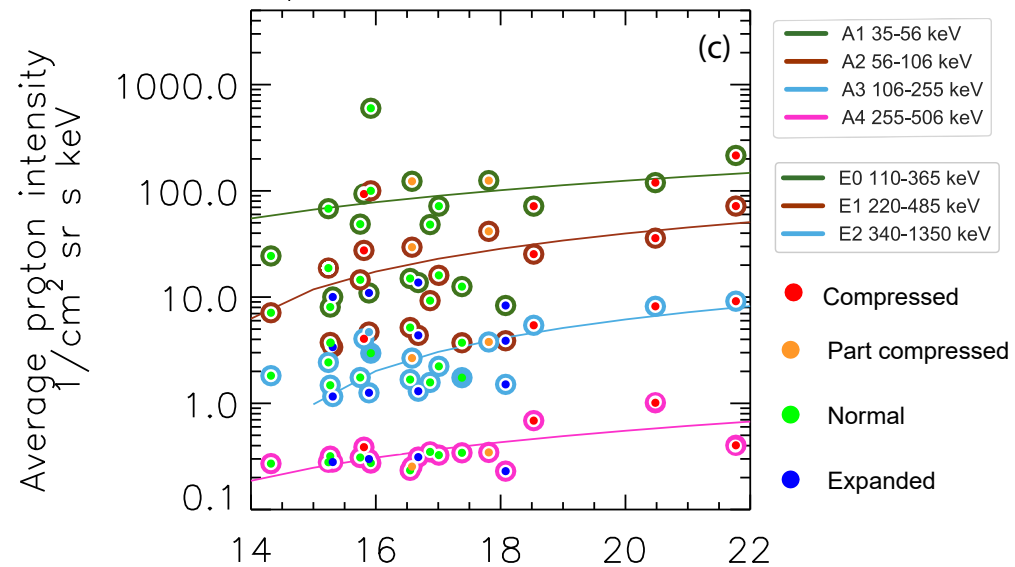
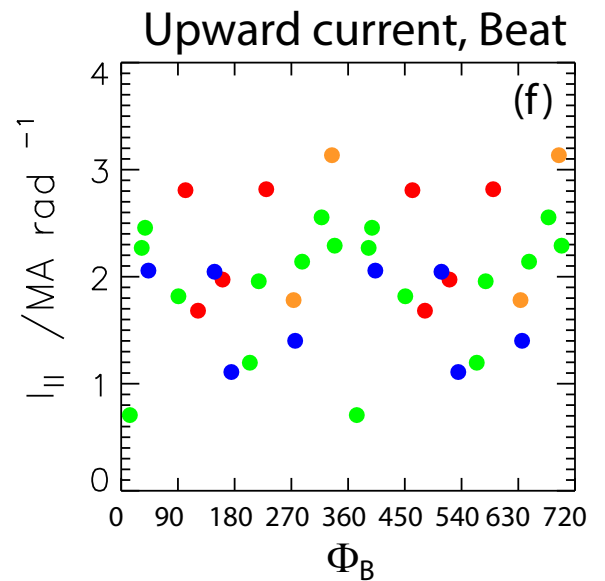
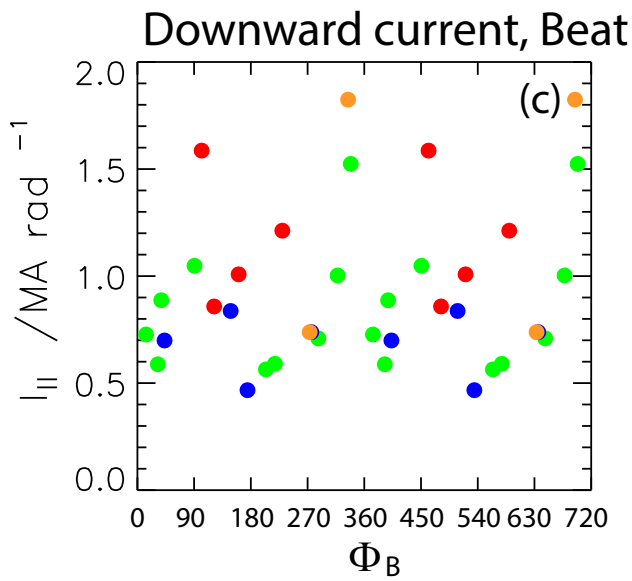
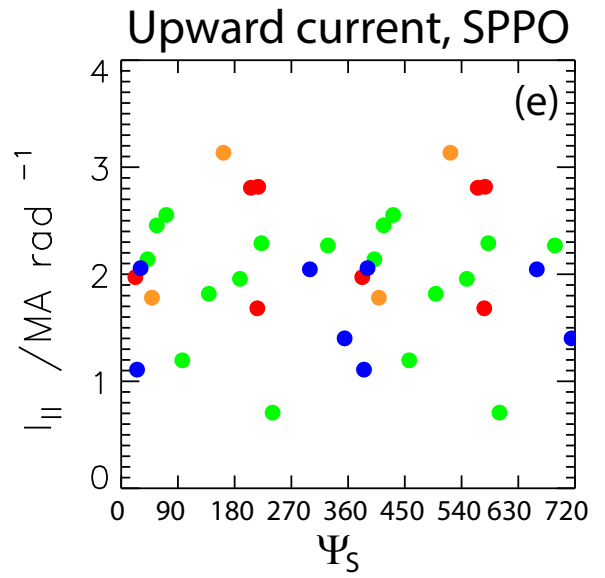
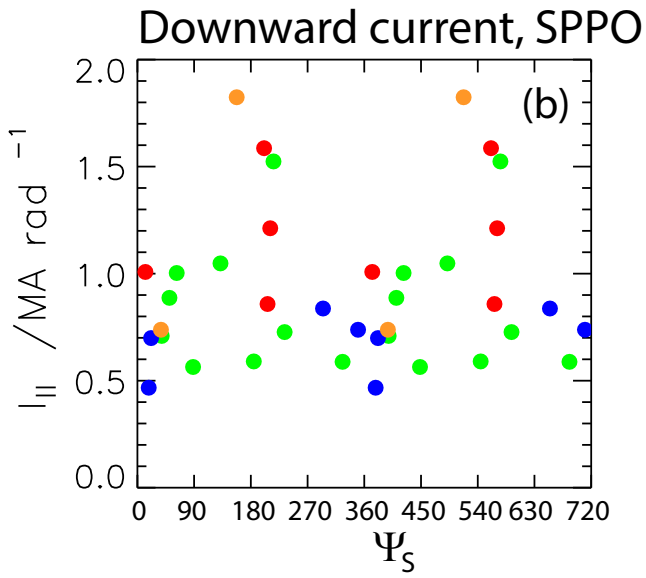
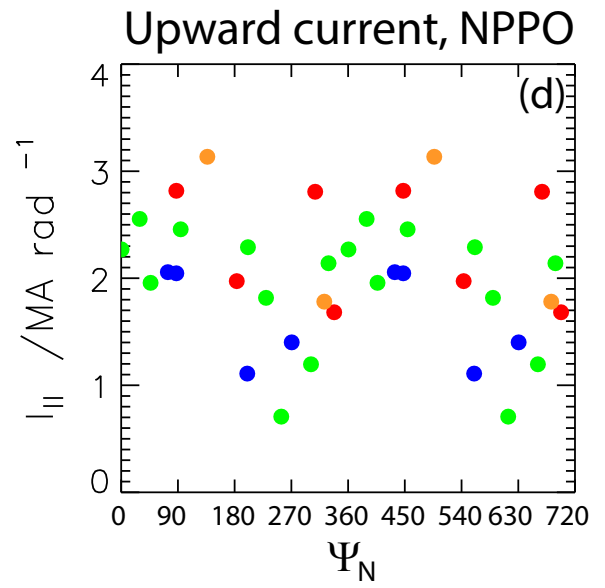
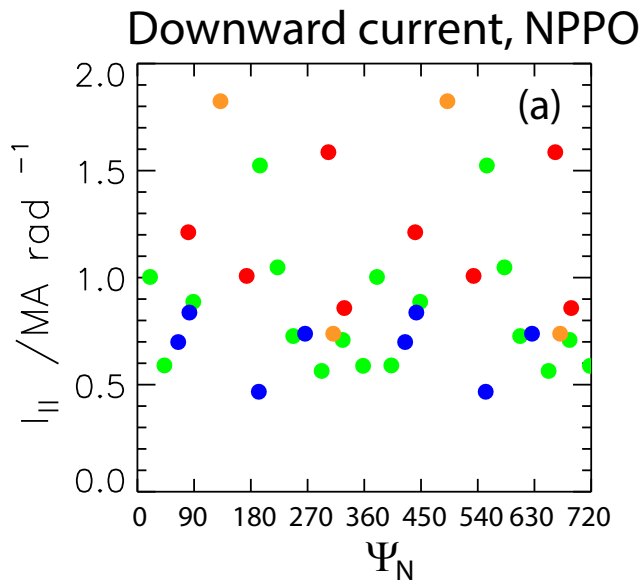


Figure 8.



● Compressed ● Part compressed ● Normal ● Expanded